Heterogeneous structure of the Northern Chile marine forearc and its implications for megathrust earthquakes

Andrei Maksymowicz,[1] Javier Ruiz,[1] Emilio Vera,[1] Eduardo Contreras-Reyes,[1] Sergio Ruiz,[1] César Arraigada,[2] Sylvain Bonvalot[3] and Sebastián Bascuñan[2]

[1]*Departamento de Geofísica, Facultad de Ciencias Físicas y Matemáticas, Universidad de Chile, Santiago, Chile. E-mail: andrei@dgf.uchile.cl*
[2]*Departamento de Geología, Facultad de Ciencias Físicas y Matemáticas, Universidad de Chile, Santiago, Chile*
[3]*Géosciences Environnement Touluse, Observatoire Midi-Pyrénées, 31400 Toulouse, France*

SUMMARY

Recent studies have proposed that nucleation zones, seismic barriers and high-slip patches of megathrust earthquakes correlate with physical heterogeneities, both in the oceanic/subducting plate and in the continental wedge. We present a density-depth model along the Nazca-South America subduction margin, from 18°S to 23°30′S, where a partial segment of this zone was ruptured by the M_w 8.2 Iquique earthquake on 2014 April 1. The density modelling and interpretation were constrained with seismic reflection profiles, published Vp-depth tomographic models and relocated seismicity. These results were used to estimate the variability of normal stress on the seismogenic contact. Our results show a heterogeneous structure for the Northern Chile marine forearc. In particular, we observed a latitudinal and longitudinal segmentation of continental wedge properties, where changes in density can be explained by changes in fracturing degree, which could have an important control on the Iquique earthquake rupture process. This study provides new insights into the analysis of large earthquakes and seismic/tsunami hazard in this active segment of the Chilean margin.

Key words: Composition and structure of the continental crust; Fault zone rheology; Gravity anomalies and Earth structure; Seismicity and tectonics; Dynamics: seismotectonics.

1 INTRODUCTION

On 2014 April 1, the M_w 8.2 Iquique earthquake ruptured a segment of the Nazca-South America subduction zone that had not been affected by large earthquakes ($M \geq 8$) since the 1868 Southern Peru and the 1877 Northern Chile megathrust earthquakes (Comte & Pardo 1991; Fig. 1a). The Iquique main shock occurred in a zone of 100 by 60 km, around a foreshock seismicity and slow-slip event that started several months before (Ruiz *et al.* 2014; Socquet *et al.* 2017). The rupture propagated to the south-east for more than 70 km, and stopped north of ∼20°30′S, where the main slip patch was concentrated (Hayes *et al.* 2014; Ruiz *et al.* 2014, Schurr *et al.* 2014, Duputel *et al.* 2015, and references therein).

In general, the published coseismic slip models, generated with different techniques and data sets, show similar characteristics, with a large and smooth slip patch located SE of the epicentre (see Fig. 1). According to the joint inversion presented by Duputel *et al.* (2015) using seismological, GPS and tsunami data, the southern half of the rupture shows more slip in comparison to the northern area. The up-dip limit of the rupture seems to be shallower in the southern region, where a westward prolongation of the coseismic slip suggests the presence of a barrier at the southern edge of the rupture (Fig. 1a).

The analysis of the gravity signal of the study zone shows that the slip pattern of the Iquique earthquake seems to be modulated by inhomogeneities and structures present both in the subducted slab and in the upper plate, as in the case of several large earthquakes in other subduction margins (Song & Simons 2003; Wells *et al.* 2003; Robinson *et al.* 2006; Mochizuki *et al.* 2008; Loveless *et al.* 2010; Sparkes *et al.* 2010; Contreras-Reyes & Carrizo 2011; Wang & Bilek 2011; Maksymowicz *et al.* 2015; Bassett *et al.* 2016). The Free-Air satellite gravity field map (Sandwell & Smith 2009) reveals that the approximate southern limit of the Iquique 2014 earthquake coincides with a strong change in offshore gravity, where an almost uniform high signal southward is separated from a lower and complex signal to the north (Fig. 1b). This large gravity change correlates well with the southern limit of the segment where the Iquique Ridge collides with the continent. To the north, the Iquique main shock slip distribution is located below a gravimetric low (Álvarez *et al.* 2015; Meng *et al.* 2015), whereas the northern limit of the earthquake spatially correlates well with the location of a local gravity high, which matches the southern border of the large Arica forearc basin (Fig. 1b). The relative size of the marine forearc basins (Iquique and Arica), and the location of the surrounding basement heights, can be interpreted from the vertical derivative of the free-air gravity signal (Fig. 2), which corresponds to a high-
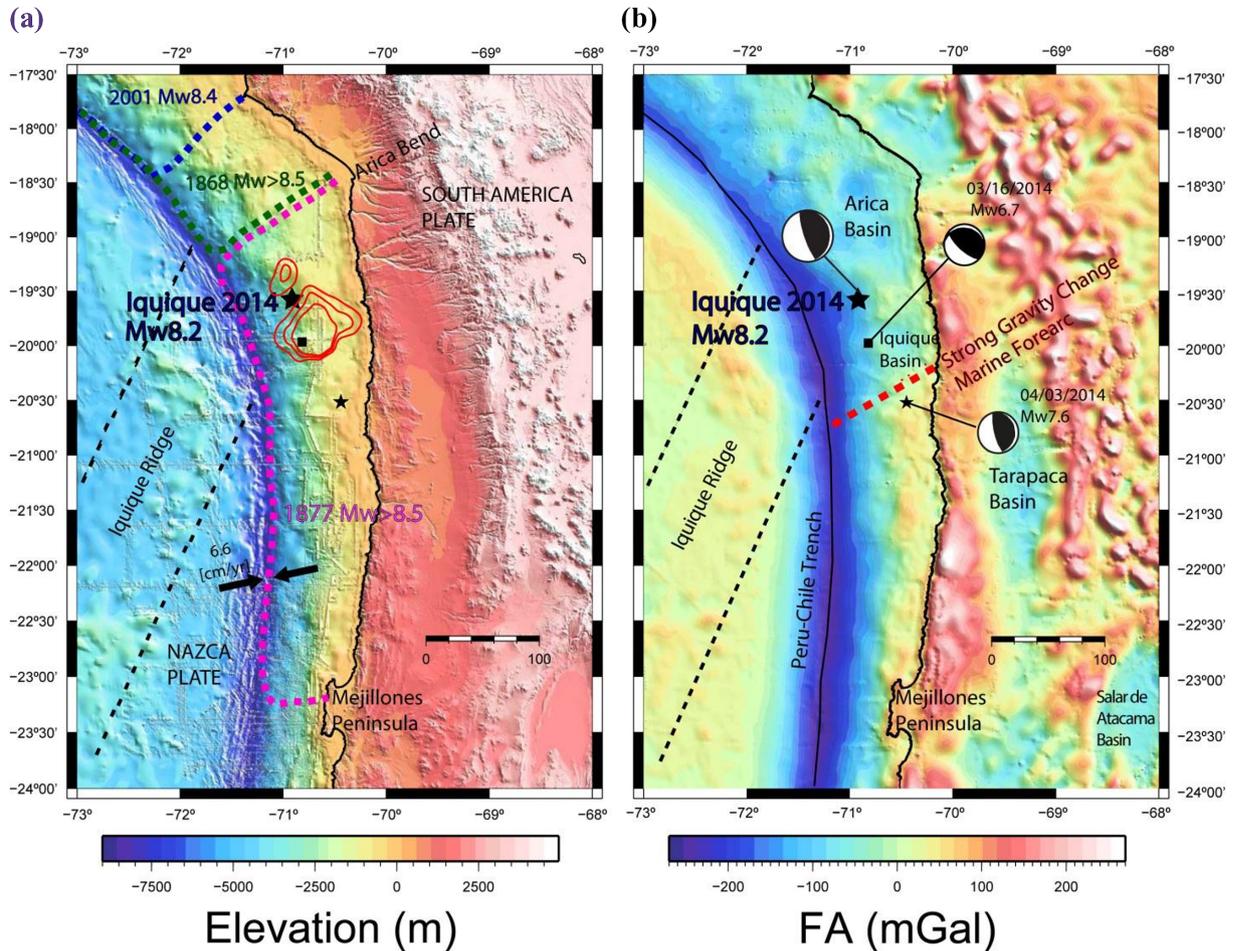
Figure 1. Tectonics and morphology of the northern Chile margin. (a) Topography and bathymetry of the study zone, large black star indicates the epicentre of the 2014 M_w 8.2 Iquique earthquake, small black star corresponds to the largest aftershock (M_w 7.7), and black square is the largest upper plate foreshock (M_w 6.7). Red lines are the slip iso-contours (2, 3 and 4 m) for the main event according to Duputel *et al.* (2015). Dotted blue, dotted green and dotted magenta lines indicate the estimated rupture areas for the large 2001, 1868 and 1877 earthquakes, respectively. Dotted black line corresponds to the approximate limits of the Iquique Ridge. (b) Merged free-air (FA) gravity grid of the satellite data (Sandwell & Smith 2009), marine gravity and onshore stations. Dotted red line indicates the strongest gravimetric change observed in the marine forearc.

pass filter of the gravimetric signal that highlights the response of shallow density variations within the crust (Blakely 1995).

The objective of this work is to obtain a quantitative evaluation of the regional impact produced by the continental wedge structure and oceanic features on the rupture process in the Nazca–South America margin (18° S–23°30′S). The density-depth models and the interpretation of seismic, seismological and bathymetric information presented here, provide a regional geophysical framework to understand the complex process of earthquake rupture in the Northern Chile subduction zone, suggesting possible scenarios for previous and future earthquakes in this portion of the margin.

2 SEISMOTECTONIC SETTING

The studied zone involves the northern Chile–southern Peru convergent margin, characterized by the subduction of the Nazca plate below South-America at a rate of 6.6 cm yr^{-1} (Angerman *et al.* 1999). North of the study area (near 18°30′S), the strike of the margin rotates abruptly, forming the Arica Bend. The tectonic importance of the Arica Bend is evidenced by counterclockwise paleomagnetic rotations of the continental crust to the north of the bend, and clockwise paleomagnetic rotation southwards (Arriagada *et al.* 2008).

The variability of the deformation field along the margin generated the Bolivian Orocline of the Andes, which is characterized by the presence of the largest plateau observed in a non-collisional subduction zone (Altiplano-Puna plateau, Isacks 1988). Along the coast, the geology of the study zone is mainly characterized by outcrops of Jurassic-Early Cretaceous volcanic/sedimentary and plutonic units associated with the Early Andean Magmatic Province (Oliveros *et al.* 2006, 2007; Charrier *et al.* 2007; and references therein). A noteworthy change in coastal geography and geology is seen at *ca.* 23–23°30′S, with the presence of Late Triassic metasedimentary and igneous rocks belonging to the Mejillonia Terrane, which represent the accretionary wedge/marginal basin of that time (Casquet *et al.* 2014)

The arid climate of the study area results in little terrigenous sedimentary flux to the trench, favouring subduction erosion (Lallemand *et al.* 1994; Clift & Vannuchi 2004). Consequently, subduction erosion has caused large-scale crustal thinning and long-term subsidence of the outermost forearc (e.g. Sallares & Ranero 2005; Contreras-Reyes *et al.* 2012).

As mentioned above, the Iquique earthquake ruptured a segment of the Nazca-South America subduction margin that had not been affected by large earthquakes since the events in 1868 and 1877
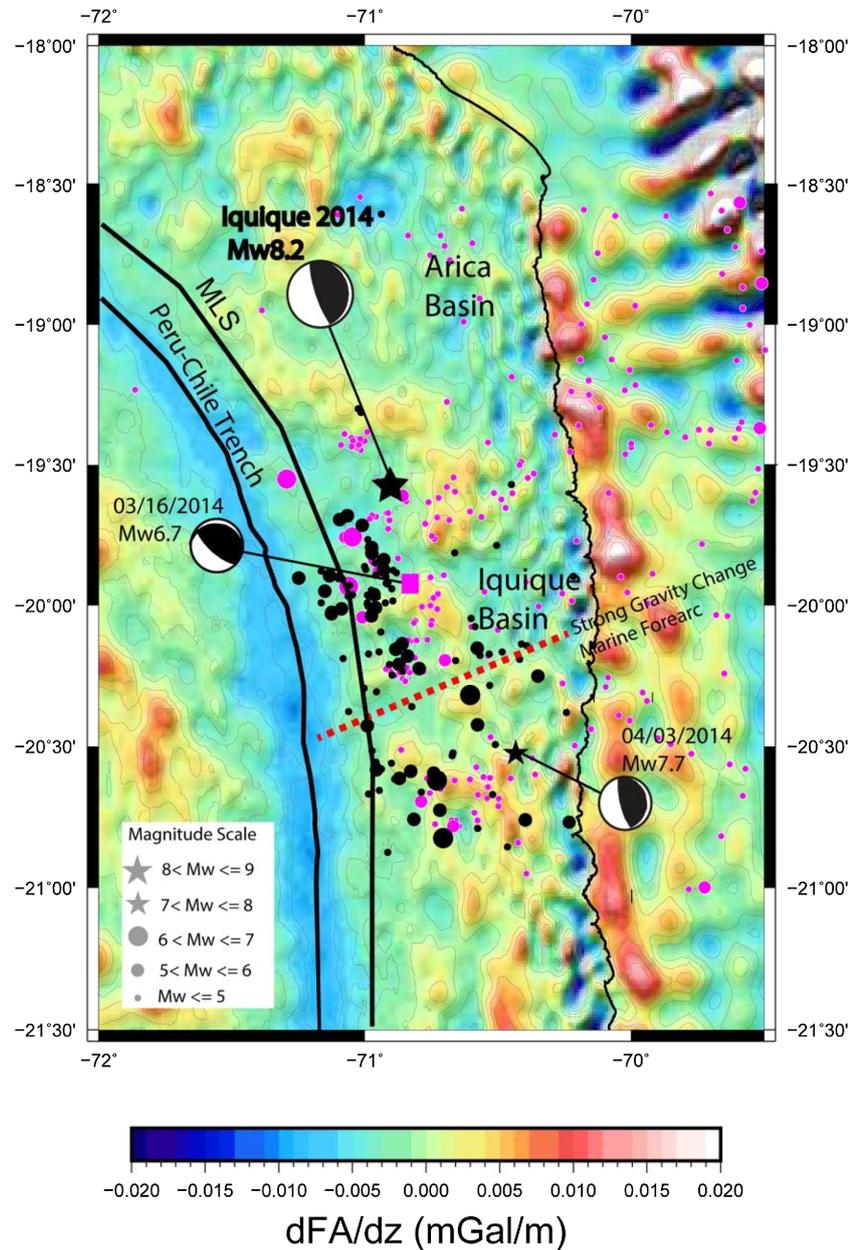
Figure 2. Seismicity associated with the 2014 Iquique Earthquake sequence and gravity anomalies. The figure includes events located by the Centro Sismológico Nacional de la Universidad de Chile from 2013 January 1 to 2014 March 14 ($M > 3$), and the relocated catalogue published by León-Ríos *et al.* (2016), which covers the period between 2014 March 15 and 2014 July 29 ($M \geq 4$). Foreshocks are shown in magenta and aftershocks in black. MLS line indicates the limit between the lower and middle slopes. The colored grid corresponds to the first vertical derivative of the free-air gravimetric signal. Dotted red line indicates the strongest gravimetric change observed in the marine forearc. Focal mechanism for the main shock (M_w 8.2), largest foreshock (M_w 6.7) and aftershock (M_w 7.7) are plotted.

(Fig. 1a). The coseismic slip was distributed between the southern limit of the Arica Basin (~19°30'S) and ~20°30'S, where a strong change in offshore gravity is observed. Existing seismic coupling models of the Northern Chile subduction margin (Metois *et al.* 2013, 2016; Ruiz *et al.* 2014; Schurr *et al.* 2014), show that the Iquique earthquake ruptured a highly coupled zone of the seismogenic contact. The same models indicate a coupled seismogenic contact south of the Iquique Earthquake, between ~21°S and ~22°30'S.

The relocated seismicity (Cesca *et al.* 2016; León-Ríos *et al.* 2016) shows that the foreshocks and aftershocks of the earthquake are distributed landwards from the limit between the lower and the

middle slopes of the continental wedge (MLS, Fig. 2). This distribution suggests an aseismic rheological behaviour of the interplate boundary in the frontal portion of the continental wedge. We point out that the foreshock sequence includes a relatively large earthquake (M_w 6.7) that ruptured inside the upper plate on 2014 March 16, with a focal mechanism and associated aftershocks that show the activation of a high-angle, east-verging structure (Ruiz *et al.* 2014; González *et al.* 2015, see Fig. 2).

Before the main shock, a sequence of earthquakes clusters and sudden increases in cumulative seismicity were observed episodically at least since July–August 2013 (Ruiz *et al.* 2014; Schurr *et al.* 2014; Yagi *et al.* 2014; Meng *et al.* 2015; Kato *et al.* 2016;

Socquet *et al.* 2017). Ruiz *et al.* (2014) interpreted this precursory period, jointly with GPS observations and microseismicity analysis, as evidence of a nucleation phase characterized by slow-slip starting 21 d before the main event. Socquet *et al.* (2017) confirmed this period of pre-seismic slow-slip events in the area affected by the main event (between 2014 March 13 and 2014 March 31), and earlier in patches around the main rupture (between 2013 July 6 and 2014 March 13). These behaviours highlight the complexities of the deformation process at the seismogenic contact, and suggest an important role for fluid pressure during the seismic cycle. In fact, the swarm sequences observed before the earthquake were characterized by the generation of repeaters (Meng *et al.* 2015; Kato *et al.* 2016), which is interpreted as an effect of high fluid pressure conditions in a specific region of the seismogenic contact (Lengline *et al.* 2014; Poli *et al.* 2017).

3 DATA AND METHODS

In order to derive the structure of the continental wedge, we generated 2-D density models by forward modelling the gravity data, constrained by seismic, seismological and bathymetric data. Available seismic reflection profiles were used to constrain the sediment thickness of the shelf and slope basins, and to characterize the general deformation style mainly in the continental shelf above the Iquique earthquake rupture zone.

3.1 Gravity data and density modelling

The density structure of the forearc was modelled along 11 profiles (P1–P11, Fig. 3), with a database consisting of marine and onshore gravity stations and satellite data. The gravimetric database includes: GEODAS gravity data, land gravity stations collected by the International Gravimetric Bureau (BGI), the land gravity stations presented by Reutter & Munier (2006) and 194 new land stations acquired by our group around Arica in 2015 (magenta squares in Fig. 3). The acquisition of new data was done with a CG-3 Scintrex gravimeter provided by the IRD-GET (Géosciences Environnement Toulouse), and elevation data were acquired using a Topcon HiperV dGPS of the University of Chile (DGF). We used the satellite grid from Sandwell and Smith (Sandwell & Smith 2009) to cover areas with scarce marine/land surface gravity data.

The elevation database (bathymetry/topography) used for the gravimetric models and interpretations corresponds to a mixed grid (Fig. 1a), which includes multibeam bathymetry data acquired during the CINCA-SO104 project (Reichert 1997), Shuttle Radar Topohtaphy Mission (SRTM) data with 90 m × 90 m pixels (Jarvis *et al.* 2008) and the Global Topography V18.1 (Smith & Sandwell 1997).

The density-depth models were generated using the GGrad free-air forward modelling schema (Maksymowicz *et al.* 2015), which allows for the calculation of the gravimetric response of a stack of layers with arbitrary shape. The densities inside each layer can be varied along the vertical and horizontal directions. To generate representative 2-D density models of the segments along the margin, the bathymetry/topography data used in the modelling correspond to an ∼40 km wide band, perpendicular to each profile (i.e. considering data extended 20 km on each side of the profile). The same averaging process was performed to obtain a representative gravity curve from the interpolated Sandwell and Smith data grid. The set of observed gravity data stations associated with each profile was selected inside the same band around the profile.

The forward modelling was constrained with the available seismological and seismic information summarized as: (1) the Slab 1.0 model (Hayes *et al.* 2012), used to constrain slab geometry mainly for depths >20 km, (2) bathymetric data at the trench, (3) the seismicity relocated by the optimization of the regional moment tensor, with a centroid depth error of about ±2.5 km (León-Rios *et al.* 2016), (4) 2-D wide-angle seismic tomographic models (Sallarés & Ranero 2005; Contreras-Reyes *et al.* 2012), used to define the geometry of the upper portion of the slab with a depth error less than 0.5 km, (5) the same 2-D wide-angle seismic tomographic models, used to estimate the density structure of the subduction zone considering empirical relations between *Vp* and density (Birch 1961a,b; Hamilton 1978), (6) the geometry of the continental Moho derived from receiver function analysis at different latitudes (Yuan *et al.* 2000; Oncken *et al.* 2003, see locations in Fig. 3), and, finally, (7) the seismic reflection lines published by Geersen *et al.* (2015) and seismic reflection lines recorded by the Chilean oil company (Empresa Nacional del Petróleo, ENAP), used to interpret the geometry of the marine forearc basins.

The inhomogeneous spatial distribution of the available information makes it necessary to apply a continuity criterion from the best constrained profiles to the neighbouring less constrained lines. In this case, the slab geometry and density obtained in profile P3 was used as an initial model for profile P2 (and afterwards for P1), and then modified to obtain the final model in this line. The same procedure was used to obtain the initial model of P7 from P6, and the initial model of P8 from P9. It is important to note that even the profiles with less constrained slab geometry (P1, P7 and P8) include geometrical restrictions such as the bathymetric depth in the trench, estimations of slope basins thicknesses, Moho depth models (profiles P7 and P8) and the geometry in the deep portion of the slab, where the depths of seismic catalogues (and the model Slab 0.1, derived from these data) are well controlled by the coverage of seismological networks. Through this procedure, we confirmed that variations in slab thickness and mantle density have a small effect on the gravity response in comparison to the shallow material of the continental wedge, at least for gravity anomalies with wavelengths shorter than ∼50 km. These previous considerations mean that the obtained density models are dependent on the accuracy of the available geophysical constraints, and that these models will be modified and improved according to the results of future experiments in the area.

3.2 Marine seismic profile analysis

We interpreted six seismic reflection lines recorded by ENAP in 1977 with a 2350 m long streamer with 48 channels and 8 airguns. We interpreted images of the final stacks that were generated in 1983 after a standard process of normal moveout (NMO). We obtained the 1-D interval velocity models in several CDP (common depth point) positions that were generated during the application of the NMO processing. Combining these velocity models, we generate a global empirical curve to convert the interpretations from two-way travel time (TWT) to depth (see Supporting Information). In all seismic lines, we identify the top of the acoustic basement, which is interpreted as the base of the forearc basins, and the main fault zones that control the deformation style of the continental wedge in the area. We complemented the analysis with the seismic reflection lines published by Geersen *et al.* (2015).
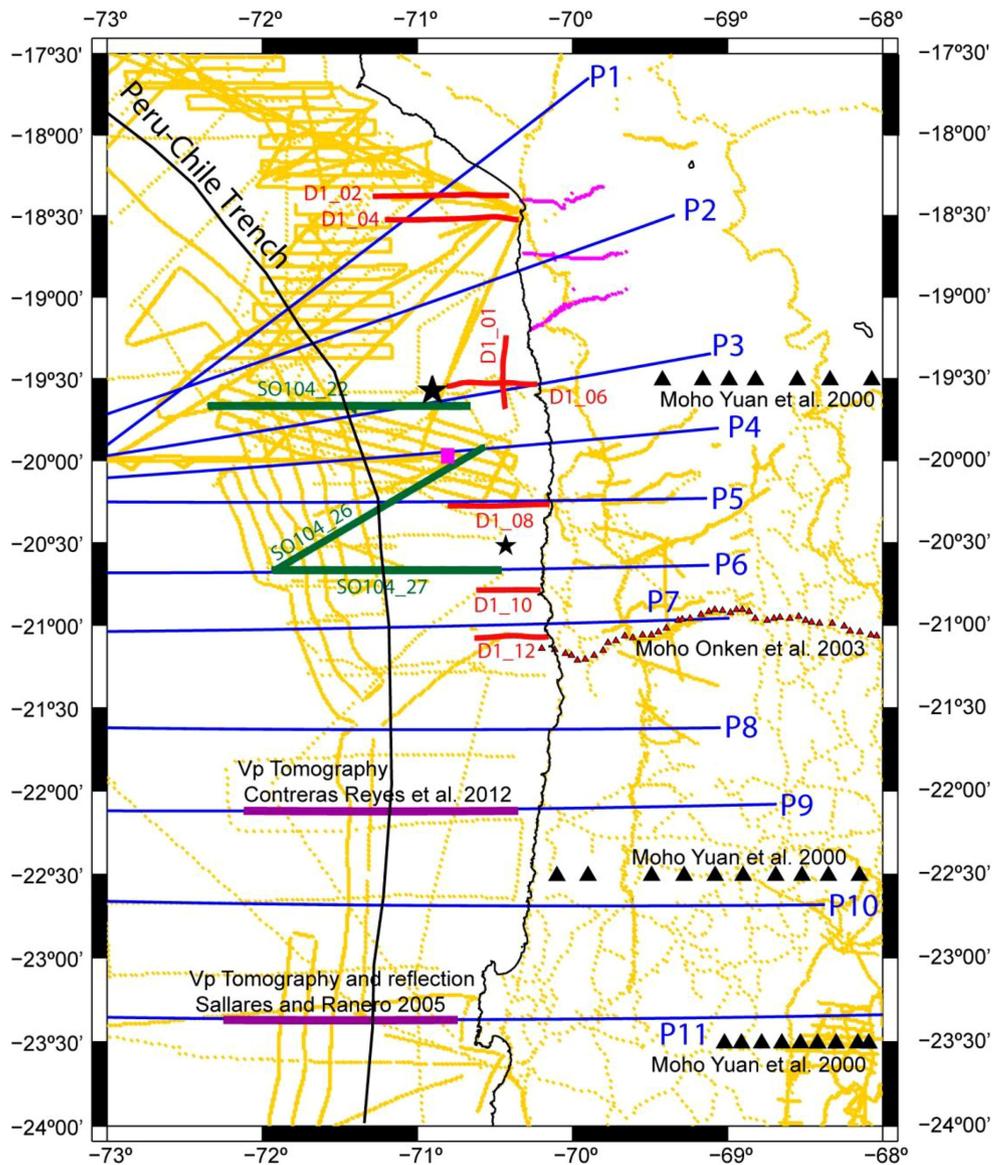
Figure 3. Distribution of geophysical data and constraints. Yellow points are available gravimetric stations in the study zone. Magenta points are 194 new gravimetric station acquired by our group in 2015. Red lines correspond to refraction seismic lines, acquired by ENAP. Green lines are the seismic reflection profiles published by Geersen *et al.* (2015). Magenta lines correspond to the wide-angle seismic profiles published by Contreras-Reyes *et al.* (2012) and Sallares & Ranero (2005) and triangles correspond to the location of Moho depth estimations, according to receiver function studies (Yuan *et al.* 2000; Oncken *et al.* 2003). Blue lines (P1–P11) are the gravimetric profiles modelled in this work.

4 RESULTS

4.1 Marine forearc basins and large crustal structures

Reflection seismic lines show the shape, distribution and internal deformation style of the shelf-basins, which, in addition to the bathymetry analysis, allows for the characterization of the main morpho-structural domains present in the marine continental wedge. Fig. 4 shows the ENAP seismic lines located around the Iquique earthquake rupture, and their location over a slope gradient grid ($|\vec{\nabla}(\text{Elevation})|$) to highlight the distribution of large bathymetric/topographic changes.

Around the zone where the Iquique earthquake occurred, the ENAP lines show that the continental shelf basins have variable shapes, with sedimentary thicknesses that, in general, increase oceanwards, reaching maximum values of <1 km. However, at

the landward edge of line SO104–26, Geersen *et al.* (2015) show that the sedimentary thickness is larger and probably increases landwards, indicating that the Iquique basin corresponds to an important depression in the continental basement. North of the studied area, the shelf basin is observed in ENAP lines D1_02 and D1_04, showing the depocentre of the Arica Basin with a sedimentary thickness of about 4 km (see Supporting Information). Therefore, the seismic reflection lines show a continental shelf characterized by small marine basins, with the exception of the well-developed Iquique and Arica basins, which are clearly associated with low free-air gravity anomalies (Figs 1 and 2). Lines S0104_22, S0104_26 and S0104_27 show slope basins that grow to the west, with maximum sedimentary thicknesses near 1 km, and, below the lower slope, a frontal wedge probably formed by sediments and/or fractured rocks (Geersen *et al.* 2015, see Supporting Information).
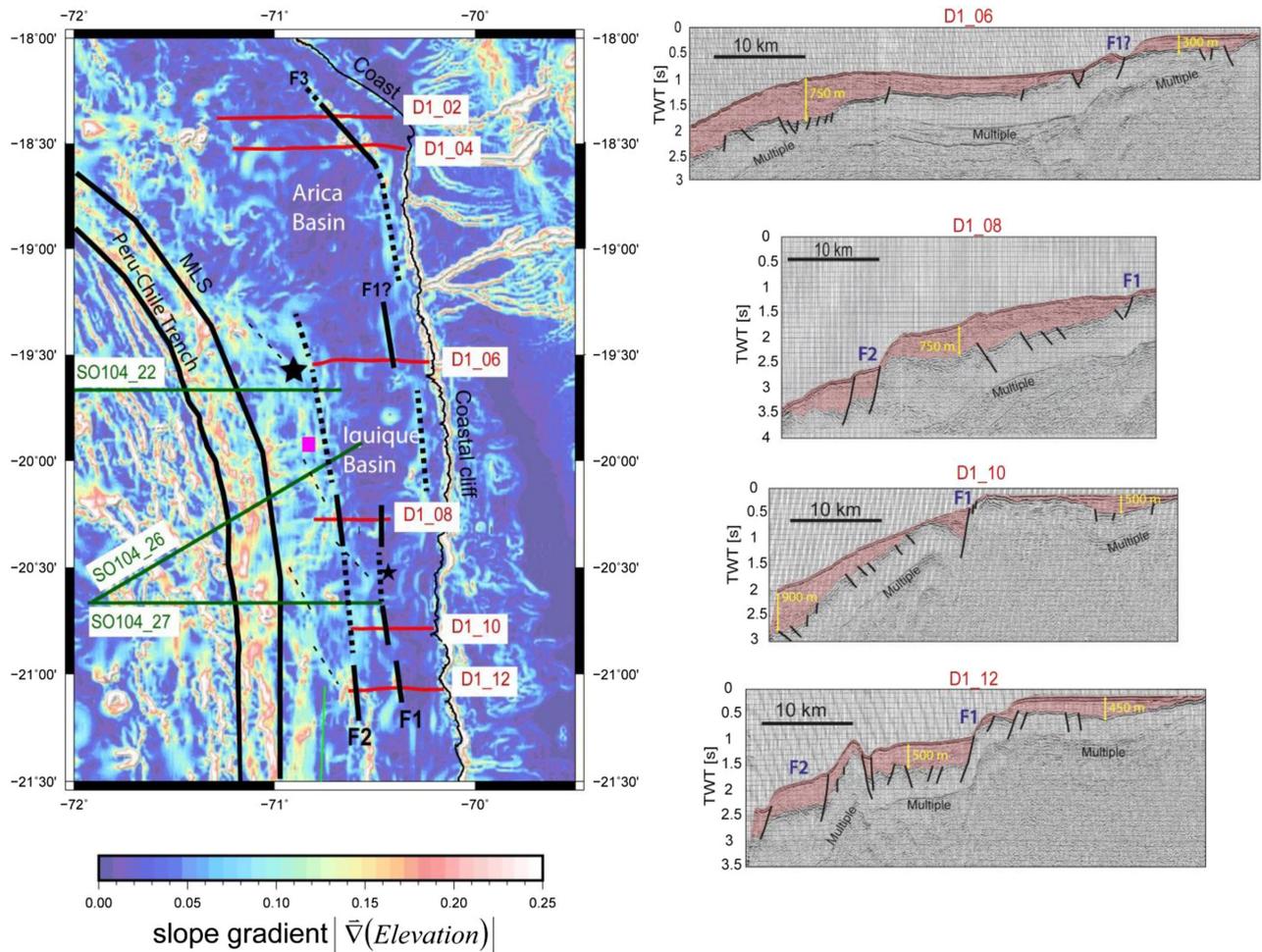
Figure 4. Structural style of the continental wedge according to seismic reflection profiles and bathymetry. Left-hand panel shows a grid of the slope gradient of the bathymetry/topography elevation. Continuous black lines indicate the structural limits interpreted in seismic profiles (F1, F2 and F3) and dotted black lines indicate possible continuity of these structural limits according to bathymetric lineaments. Thin dotted black lines highlight a secondary set of northwest-striking liniments. Red lines correspond to the location of ENAP seismic reflection profiles and green lines are the SO104 seismic reflection profiles. The epicentres of the main shock (M_w 8.2) and the large foreshock and aftershock (M_w 6.7 and M_w 7.7) are indicated as in previous figures. Right-hand panels are examples of interpreted ENAP seismic lines, where the sedimentary fill is highlighted in orange and the fault zones are indicated in black. The sedimentary thickness in several points of the forearc basins is indicated in yellow.

The general deformation style observed in the seismic lines is characteristic of a margin affected by subduction erosion (Fig. 4), where normal faulting is generated by the collapse of the continental wedge in response to material removal in the lower part of the upper plate (von Huene & Scholl 1991; Sallares & Ranero 2005; Vannucchi *et al.* 2012). Accordingly, the slope gradient image presents numerous bathymetric lineaments parallel to the margin in the lower and middle slopes, and a second set of smaller northwest-striking structures.

The area where the Iquique earthquake broke shows at least two major deformation zones where sediment thickness decreases abruptly, and where the continental basement presents large offsets (see seismic profiles in Fig. 4). These zones (F1 and F2), can be observed in several seismic lines, which, in addition to coincident bathymetric lineaments, suggests a north–south continuity of this continental structure. These deformation zones are expressed near the surface as large landward-verging crustal faults. Evidence of the tectonic importance of these deformation zones is the correlation between F2 and the shelf-break, which marks the large regional geometry change of the marine continental wedge. Additionally,

the vertical offsets of the faults observed in F1 and F2 are similar to those observed in the coastal cliff, which is a first-order feature of the Andean forearc in the northern Chile margin (Contreras-Reyes *et al.* 2012; Armijo *et al.* 2015; Melnick 2016). North of the Iquique rupture zone, the ENAP seismic profiles show evidence of contractional deformation superimposed over the general normal faulting style inside the Arica Basin (see Supporting Information), thus evidencing stress–strain changes along the margin.

As shown in the following sections, the sedimentary thickness obtained from nearby reflection seismic profiles can be included as a constraint for the forward gravity models. This improves the quality of the density model below the forearc basins.

4.2 Density structure of the continental wedge

Fig. 5 shows the 2-D density models obtained along the gravity profiles (P1–P11), by forward modelling the observed gravity data. In order to highlight details of the continental wedge and the upper portion of the subduction zone, we show segments of the density models extended between 50 km seawards of the trench axis and
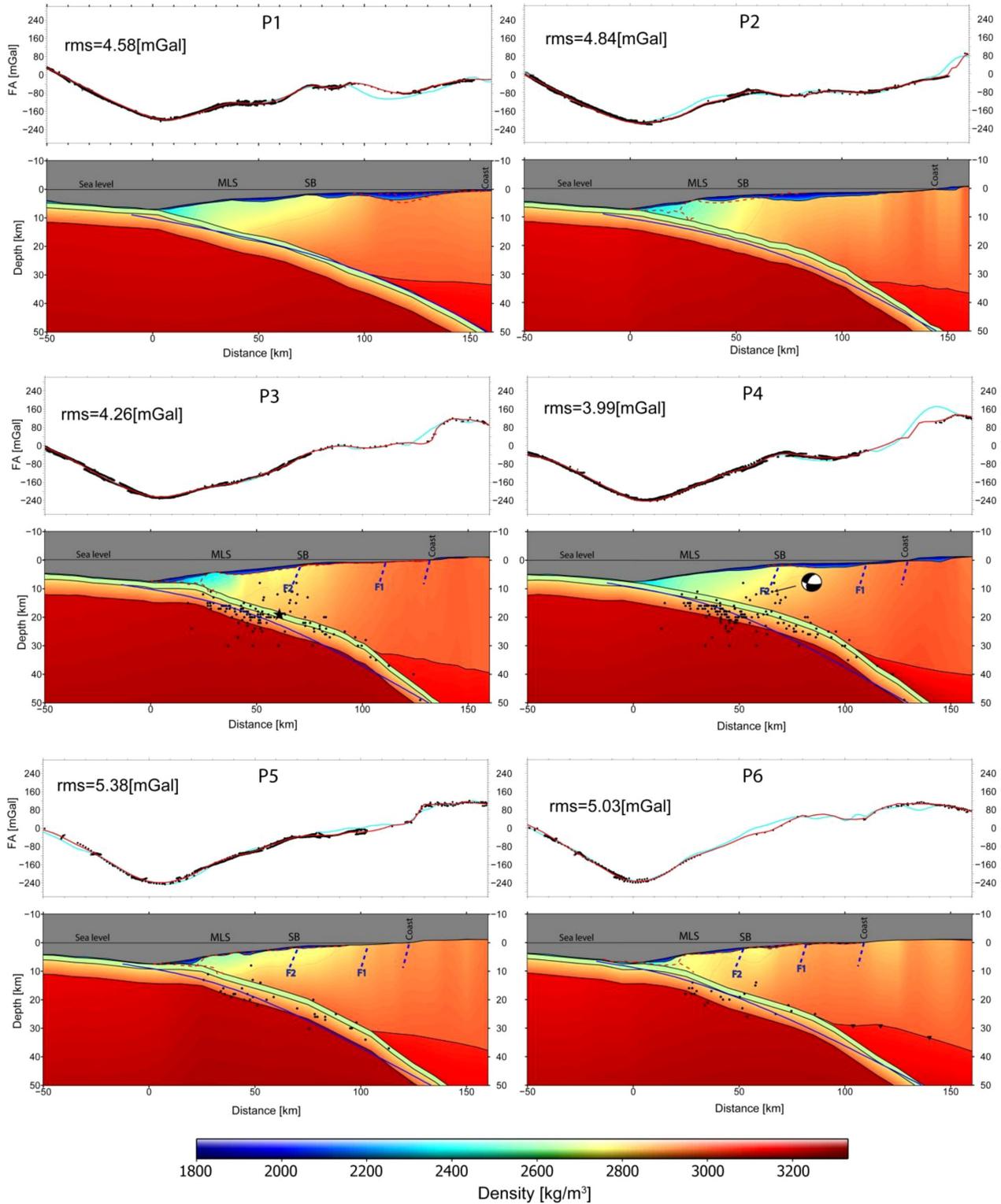
Figure 5. Density-depth models of the gravity model profiles. For each profile (P1–P11), the upper panels present the observed gravity in the gravimetric stations (black dots) and cyan lines show the complementary Sandwell and Smith satellite data. Red lines correspond to the modelled free-air gravity. The lower panels present the 2-D density model. Dotted red and magenta lines present the sediment/basement discontinuities observed in the nearest reflection or the wide-angle seismic profile. Inverted black triangles are the Moho depths estimated by receiver functions with an error of about ±5 km (see locations in Fig. 3). Blue lines are the slab geometry according to the Slab1.0 model. Black dots are relocated seismicity, and black star in profile P3 is the Iquique earthquake hypocentre. The focal mechanism of the M_w 6.7 foreshock is shown in profile P4. Dotted lines are the main structures (F1 and F2) interpreted in reflection seismic profiles.
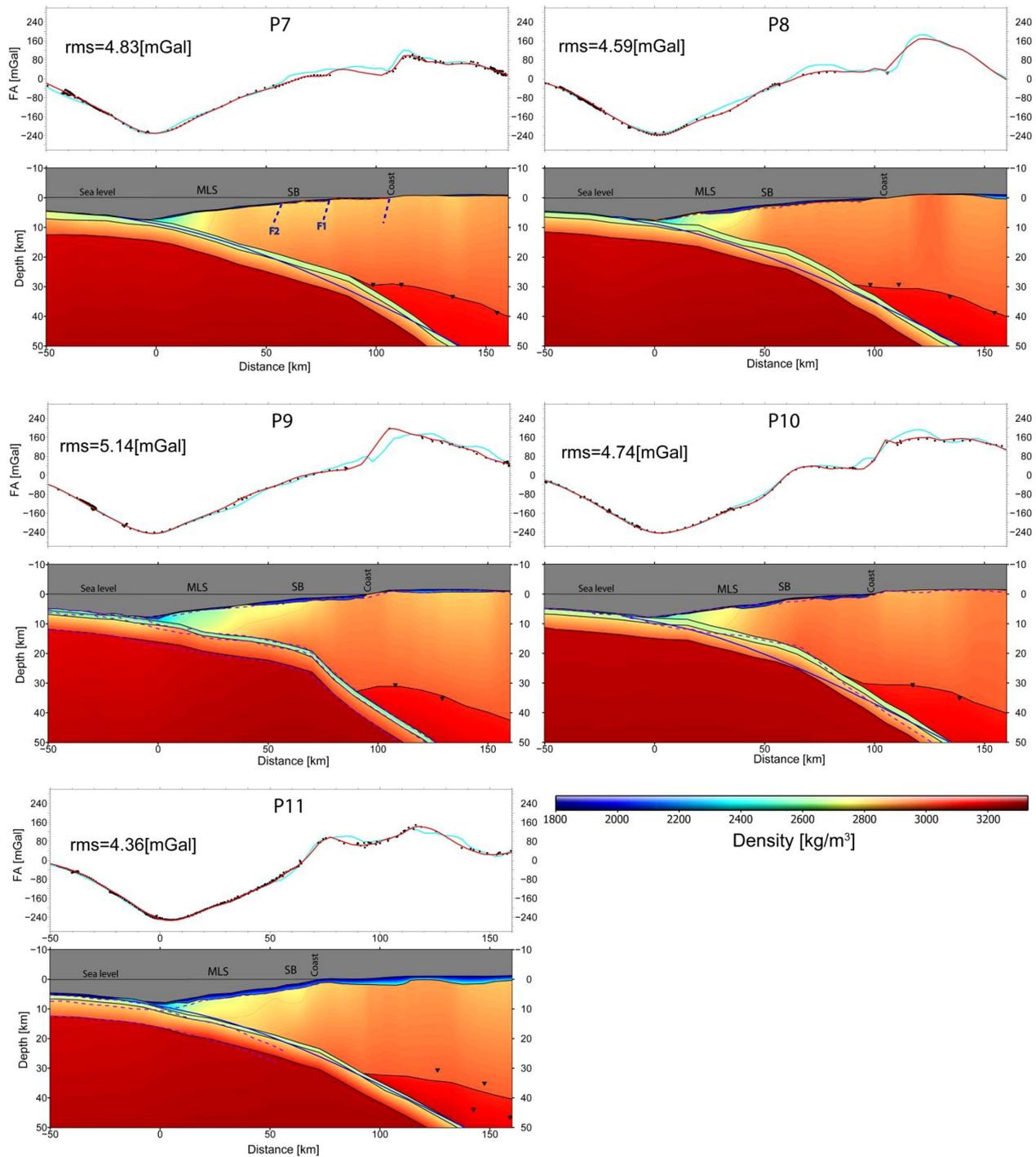
Figure 5. (*Continued.*)

160 km landwards of the trench (see the complete gravity models in the Supporting Information). The upper panels in Fig. 5 show the observed free-air gravity data (black dots) and the predicted gravity curve (red line). The root mean square error (between modelled and observed data) is lower than 5.4 mGal, which represents ∼1.9 per cent of the total amplitude of the observed gravity signal. This indicates that the density models are clearly possible solutions for the density structure in the region. In general, a good correlation between *in-situ* measurements and satellite data is observed for the marine portion of the profiles, but the discrepancy between inland gravity stations and satellite data highlights the importance of onshore gravity campaigns to model the continental structure of the forearc and continental shelf.

The subduction slab geometry obtained (lower panels in Fig. 5) shows an increase in slab subduction angle at ∼20–25 km depth, which is consistent with the relocated seismicity of León-Ríos *et al.* (2016) in profiles P3, P4, P5 and P6, and with the wide-angle seismic velocity-depth models in profiles P9 and P11 (Sallarés & Ranero 2005; Contreras-Reyes *et al.* 2012; see Figs 3 and 5). Assuming similar density variations within the continental wedge, slab and

mantle, in reference to the adjacent profiles, the forward modelling indicates that the increase in slab subduction angle is also present in profiles P2, P7, P8 and P10. Flexural models worldwide show that the angle of the interplate boundary should be <15 deg near the trench to be consistent with the observed shape of the outer rise (e.g. Hunter & Watts 2016; Contreras-Reyes & Garay 2018). Thus, we include a low initial angle of subduction, based on bathymetric and active seismic data constraints, and a steeper angle of subduction landwards of the shoreline based on seismological and gravimetric constraints.

The density structure of the continental wedge shows a general landwards increase in density. In the frontal part of the continental wedge (approximately below the lower slope), all models show densities lower than 2400 kg m^{-3}, which are indicative of the presence of debris and/or highly fractured rocks (Contereras-Reyes et al. 2011; Tréhu et al. 2012; Maksymowicz et al. 2015; and references therein). To the east, approximately below the middle slope [i.e. between the upper limit of the lower slope (MLS) and the shelf-break (SB)], the modelled profiles show densities lower than 2700–2800 kg m^{-3}. Assuming a similar lithology for the continental basement, this second unit is interpreted as moderately fractured basement rocks, in comparison with the high density basement observed to east (higher than 2900 kg m^{-3}; Contereras-Reyes et al. 2011; Tréhu et al. 2012; Lücke and Arroyo 2015; and references therein). The coastal geology is similar along the study zone (mainly outcrops of volcanic/sedimentary units and plutonic rocks, see above), which suggests a seaward continuity of the same lithology. Therefore, regional changes in the continental wedge density are interpreted mainly as regional changes in the deformation style, rather than the effect of local changes in lithology, which, in any case, could control gravity variations at smaller scales.

The projection of the relocated seismicity to the nearest modelled gravity profiles P3, P4, P5 and P6, leads to interesting correlations. The upper limit of the interplate/intraslab seismicity (located around 20 km landwards from the trench) coincides with the presence of low densities in the frontal part of the continental wedge, and the large amount of interplate/intraslab seismicity is located below the zone of intermediate continental densities, between MLS and SB (see P3 and P4 in Fig. 5). The intraplate seismicity inside the continental wedge is located near the SB position, and seems to follow in depth the vergency of the large faults observed at the surface (associated with tectonic limit F2). Thus, profile P4 shows a remarkable spatial correlation between morphological and structural features (see Figs 2, 4 and 5). Particularly, a lateral basement density change (from 2600 to 2800 kg m^{-3}) correlates well with the location of the SB along the profile, which in turn coincides with the location of F2, and with the hypocentre of the M_w 6.7 intraplate foreshock (Ruiz et al. 2014).

Comparing the density models obtained along the profiles, we observe that densities are systematically lower in profiles P1–P5 when compared to other profiles located south (i.e. latitude 20°30′S corresponds to a change in the continental structure along the margin). To clarify this N–S variation (and also the W–E characteristics of the models), we studied the vertical average density in the marine continental wedge (from the seafloor to the top of the slab) along the modelled profiles. Fig. 6(a) presents the variation of this parameter as a function of horizontal distance to the trench (for each profile), and Fig. 7(a) shows a map with an interpolated grid of vertical average density in a band extended from the trench to ~100 km landwards. In front of the continental wedge (i.e. below the lower slope), the average density shows a rapid landward increase, defining a possibly unconsolidated/highly fractured unit. However, the

landward density increase is less marked in the northern profiles (P1–P5) than in the southern profiles (P6–P11), which means that the width of the frontal unit is smaller south of 20°30′S. To the east, below the middle slope, the landward increase in density is relatively lower, showing a big contrast with the frontal unit. Below the continental shelf, the densities present a very smooth increase landwards, reaching values over 2900 kg m^{-3}. As we can see in Figs 6(a) and 7(a), both the middle slope and shelf present lower average densities in the northern portion of the studied zone (profiles P1–P5), compared to those obtained southwards.

Figs 6(b) and 7(b) present the estimations for vertical load over the interplate boundary as a function of horizontal distance from the trench, and as an interpolated grid, respectively. This parameter indicates the vertical stress generated at the base of columns extended between the Earth surface and the interplate boundary, i.e. it also includes the weight of the water column in the zone of the marine forearc. These figures show relevant differences between vertical loads at different profiles. In the zone of the frontal unit, below the lower slope, a complex latitudinal variability is observed with values, in general, lower than 300 MPa. Vertical loads increase below the middle slope, and most profiles show a similar behaviour except for P6, P7 and P11, which have vertical load values up to 150 MPa higher than those observed in other profiles (see Fig. 6b). To the east, the vertical load pattern changes below the continental shelf, showing values systematically higher in the northern profiles (P1–P5) in comparison to the southern region (P6–P11). Then, according to the density models, the Iquique earthquake ruptured a zone where the vertical load over the contact is lower than that observed in the segment extended south of 20°30′S.

4.3 Sensitivity of the continental wedge density model

The trade-off between density and depth of a specific portion of the model is the main source of uncertainties. However, the consideration of several constraints for slab geometry, continental Moho depth, mantle and continental density variability (Figs 3 and 5) ensure that the obtained results are, at least, a consistent solution fitting the available geophysical information acquired for decades in the zone, which highlights the relevance of the obtained model.

As we can see in Fig. 5, profiles P4 and P9 are representative of the two opposite gravity domains determined in the zone (northern low gravity in the marine forearc, and high marine gravity in the southern segment), and show large differences in slab geometry, supported by independent seismological and seismic constraints (note that the slab geometry in other profiles is similar to that seen in P4 or P9). Then, to evaluate the effects of a large perturbation in the obtained models, we study the variability of the estimated average density and vertical load when their slab geometry is interchanged. Fig. 8 shows the results of this test. The theoretical response of the preferred model is used as data (black points in Figs 8a and b) and modified models of P4 and P9 are obtained interchanging their slab geometries and modifying their continental wedge densities to adjust the gravity response. Figs 8(c) and (d) show that the effect of these large modifications (in comparison to the variability observed between adjacent profiles) is only an increase in average continental wedge density and vertical load in line P9, and a decrease in average density and vertical load in profile P4. All characteristics identified previously in the original models are retained in the modified solutions, such as higher densities in profile P4 compared to P9, differentiated landward density gradients below the lower slope,
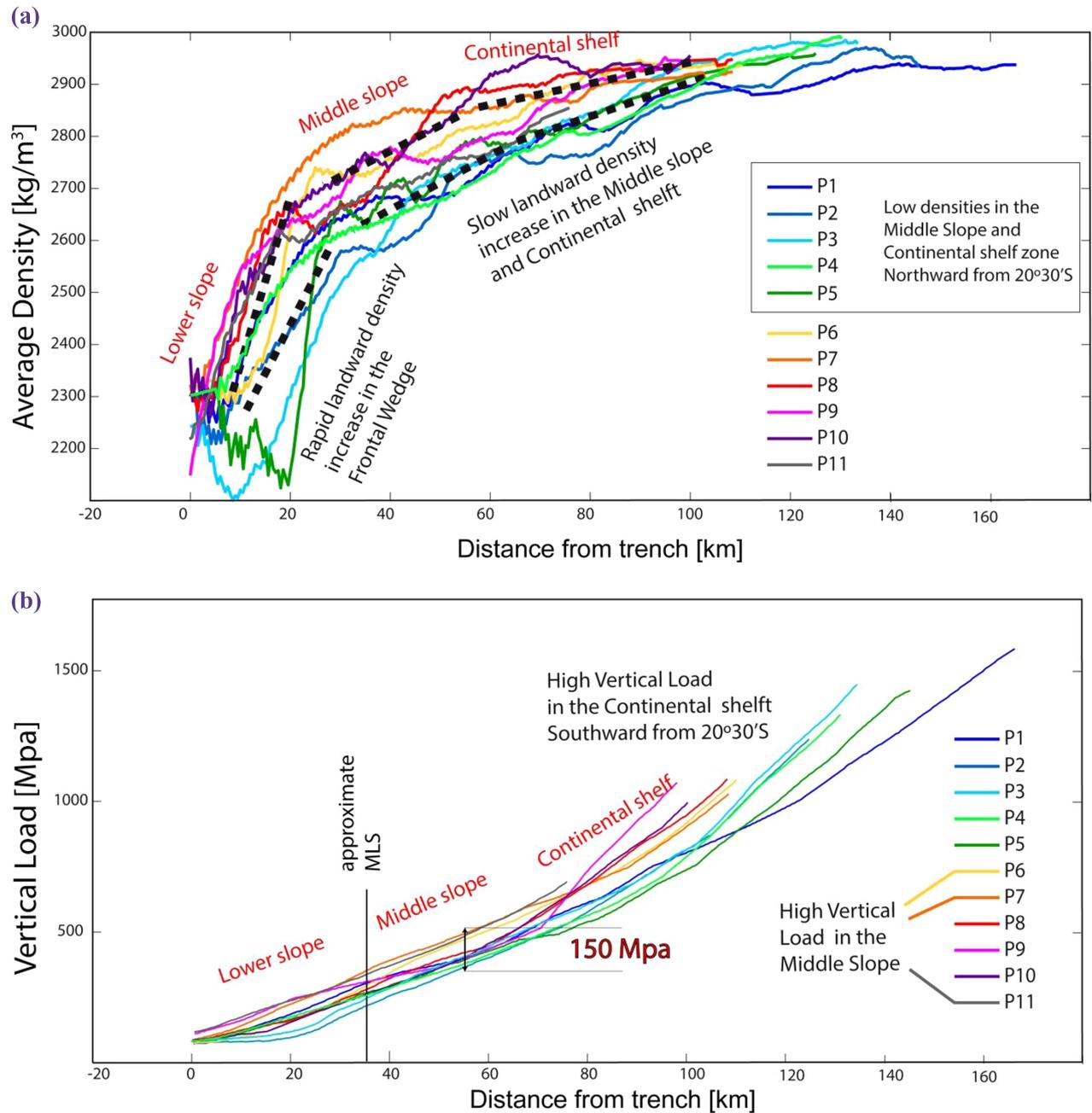
(a)

(b)

Figure 6. Average density and vertical load calculated over the interplate boundary along the density models. (a) Vertical average density of the continental wedge as a function of distance from the trench. Dotted black lines highlight the changes in the horizontal gradient of density averages. (b) Vertical load over the interplate boundary as a function of distance from trench.

middle slope and shelf, high vertical load in the shelf zone of pro-file P9, etc. This test shows that the main features recognized in the model respond primarily to large changes in the gravity signal, and that they are not critically controlled by the independent constraints. In fact, additional tests to estimate the magnitude of the gravimetric response as a function of changes in slab geometry and continental wedge density (see Supporting Information), show that changes in slab geometry around ±5 km in depth require modifications smaller than 50 kg m^{-3} in the vertical average densities, to fit the observed gravity. In summary, all the characteristics recognized previously in the preferred models can still be found in the modified solutions.

5 INTERPRETATIONS AND DISCUSSION

The results present a regional view of the northern Chile margin, where the physical parameters and tectonic features of the continental wedge and the subducted slab are related to the seismotectonics of the Iquique earthquake. In this section, we discuss possible explanations for the modelled parameters, and some implications for seismicity and the seismic cycle.
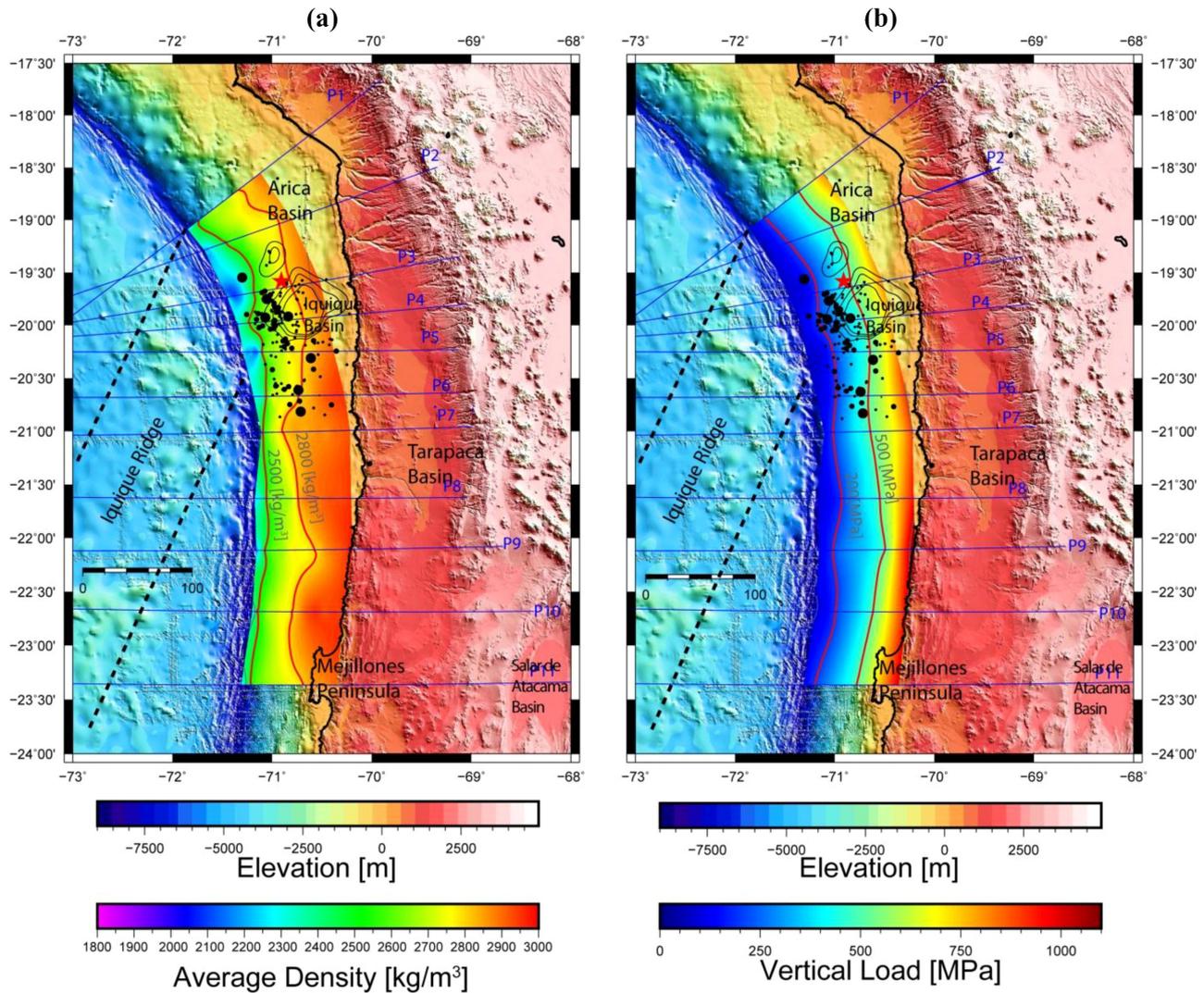
Figure 7. Maps of the average density and vertical load over the interplate boundary. (a) Interpolated grid of vertical average density of the continental wedge in the band extended from the trench to ~100 km landwards. Red star indicates the epicentre of the main shock, black dots are the foreshocks and aftershocks epicentre re-located by León-Ríos *et al.* (2016). The slip iso-contours (2, 3 and 4 m), in black, correspond to the model of Duputel *et al.* (2015) for the Iquique earthquake rupture. Continuous red lines depict the density iso-contour (2500 and 2800 kg m^{-3}). (b) Interpolated grid of vertical load over the interplate boundary in the band extended from the trench to ~100 km landwards. Other elements are the same that in (a). Continuous red lines depict the vertical load iso-contour (200 and 500 MPa).

5.1 Longitudinal tectonic segmentation of the marine forearc

The analysis of the results in a trench-perpendicular direction allows us to generate a schematic interpretation summarized in Fig. 9(a). The frontal portion of the continental wedge is formed by low-density material, which becomes denser landwards. Previous works in the northern Chile margin show the presence of a small frontal prism formed mainly by sedimentary debris eroded from the continental slope, which is a common feature in erosive margins (Clift & Vannucchi 2004). This frontal prism is ~5 km wide at the latitude of the Mejillones Peninsula (Sallares & Ranero 2005), and ~10 km wide at the latitude of profiles P3, P5 and P6 (Geersen *et al.* 2015). According to our density model, the continental wedge landwards of the frontal prism maintains a rapid density increase up to the approximate limit between the lower and middle slopes (MLS, Figs 5, 6 and 9). Therefore, the structure of the frontal portion of the continental wedge (~20–30 km wide) is explained by the rapid

landward process of compaction within the frontal prism, followed by the rapid landward decrease in fracturing of the continental basement below the lower slope. The presence of this frontal unit in all gravity models confirms, for the entire studied zone, the observation of Contreras-Reyes *et al.* (2012) at the latitude of Tocopilla (P9), where the frontal part of the continental wedge (~25 km wide) is characterized by seismic velocities lower than 5 km s^{-1}, and interpreted in terms of hydrofractured material related to subduction erosion.

Landwards from the MLS break, the continental wedge below the middle slope and the continental shelf presents average densities higher than 2500 kg m^{-3}, which increase slowly landwards (Figs 6a and 7a). In contrast to the frontal unit, this pattern suggests a decrease in porosity and/or fracturing within the continental basement. This landward increase in average density can be explained partially by the gradual increase in density in the deeper portions of the wedge. However, the change in the trend around the location
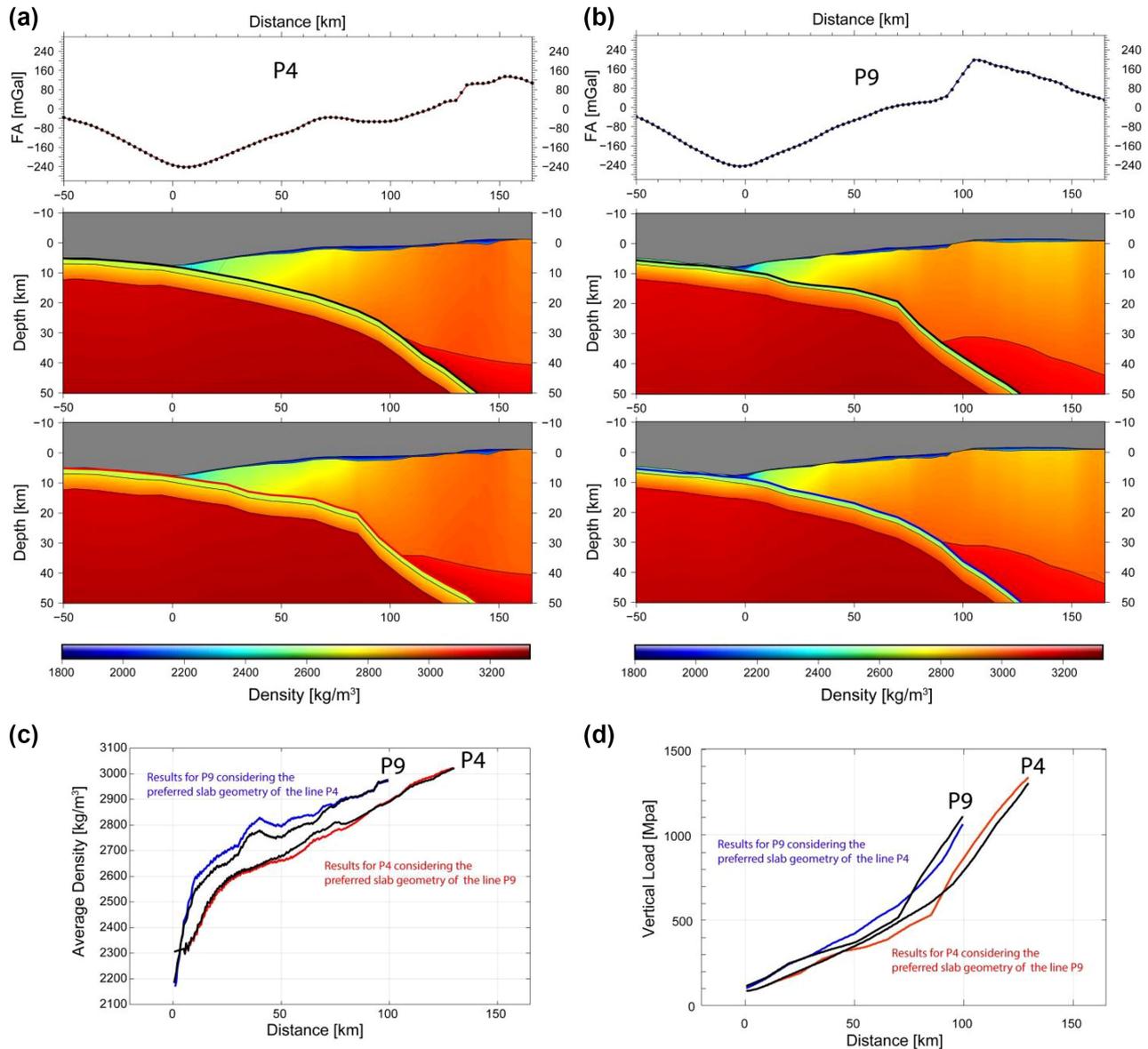
Figure 8. Sensitivity analysis for the average density and vertical load. (a) Black dots in the upper panel are the theoretical gravity response of the preferred density model for line P4 (central panel). Red line is the gravimetric response of an alternative model (lower panel), which consider the slab geometry obtained for the line P9. (b) Black dots are the theoretical gravity response of the preferred density model for the line P9 (central panel). Blue line is the gravimetric response of an alternative model (lower panel), which consider the slab geometry obtained for the line P4. (c) Average density curves. Black lines correspond to the preferred models of the profiles P4 and P9. Red and blue lines are the results for the alternative models [lower panels in (a) and (b)]. (d) Vertical load over the interplate boundary. Black lines correspond to the preferred models of the profiles P4 and P9. Red and blue lines are the results for the alternative models [lower panels in (a) and (b)].

of the SB (about 60 km landwards from the trench) is clear evidence for the correlation between wedge morphology and density structure.

We interpret the horizontal density gradients of the continental wedge as a landward decrease in fracturing of the continental basement. As such, the fluid content within the wedge should increase towards the trench, favouring its hydrofracturing and the generation of both aftershock and foreshock seismicity.

5.2 Latitudinal segmentation of the marine forearc

A latitudinal comparison of the results shows a first-order segmentation of the Chilean continental wedge along the northern

Chile margin (Fig. 9b). North of ∼20°30′S (where the strongest change in offshore gravity is seen), the average density of the wedge below the middle slope and the shelf is lower than that observed to the south. This shows that the decrease in free-air gravity anomaly to the north responds to a bathymetric change, but also to a general decrease in continental wedge density (i.e. it corresponds to a morphological and structural change in the continental wedge). The frontal zone of the continental wedge shows a rapid landward density increase south of ∼20°30′S, which evidences a narrowing of the frontal, fractured sedimentary rock south of this limit.

A complete explanation of the density, structural and morphologic segmentation is difficult due to the incomplete understanding
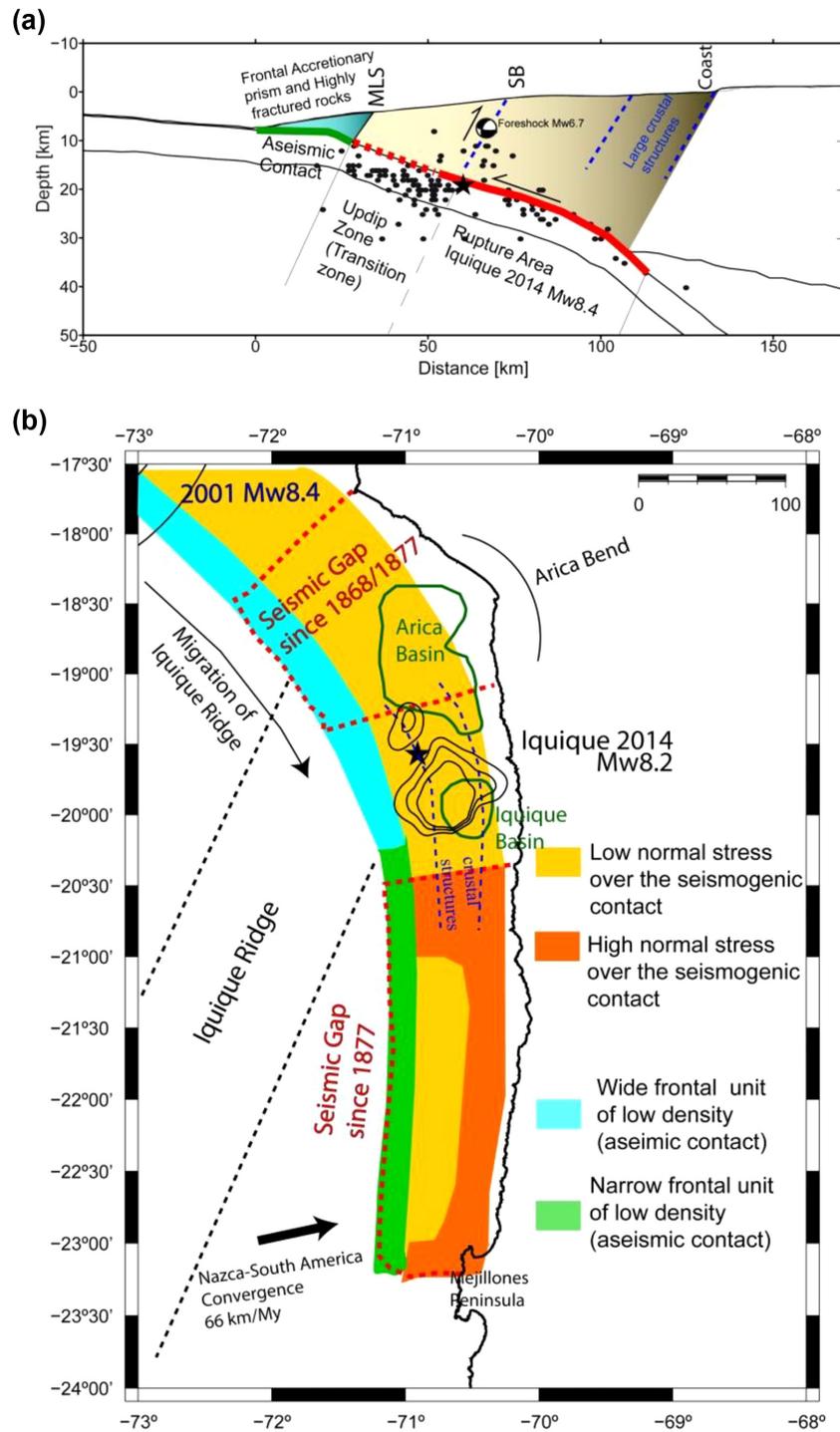
Figure 9. Structural and seismotectonic interpretation of the study zone. (a) Schematic profile, perpendicular to the trench, of the Iquique earthquake rupture zone. (b) Schematic map of the obtained physical parameters and tectonic features. Black star corresponds to the Iquique earthquake epicentre, and thin black curves are the iso-contours of the coseismic slip according to Duputel *et al.* (2015). Dotted red lines indicate the current seismic gaps in the studied zone, green lines outline the extent of large marine forearc basins.

of the stress–strain fields and the rheology of the margin. Considering these uncertainties, some explanations can be suggested in relation to important geodynamic processes observed in the area. Around the large Arica Basin, the Andean margin rotates from a northwest–southeast strike at the southern Peru region, to an almost north–south direction at the Northern Chile zone (Arica Bend). This

remarkable margin curvature should generate a complex stress–strain field in the crust, favouring pervasive deformation, fracturing, subsidence and tearing (Bonnardot *et al.* 2008; Madella *et al.* 2016). Furthermore, the hypocentre catalogue of the CSN (Centro Sismológico Nacional de la Universidad de Chile) shows that the amount of seismicity in the zone of the Arica Bend is lower than in other regions of the studied zone during the 2008–2014 time period

(see Supporting Information and Metois *et al.* 2016), suggesting an anomalous rheology for the seismogenic zone (at least below the shelf). These stress–strain particularities can explain the presence of the large forearc Arica Basin, and a general decrease in crustal density of the continental wedge.

Another important process observed in the studied area is the subduction of the Iquique Ridge north of ∼20°30′S (Figs 1, 8 and 9b). The strike of this wide feature is highly oblique to the trench in the Northern Chile region, which, in addition to the current convergence direction (Angermann *et al.* 1999), generates a rapid southward migration of the Iquique Ridge-trench intersection point (around 130 km my^{-1}). The continental wedge between Arica ∼18°S and ∼20°30′S was thus only recently affected by the subduction of the Iquique Ridge (starting at *ca.* 2 Ma).

Due to the disrupting effect of seamount subduction, the complex fracturing generated in the upper plate during the process, and the continental wedge collapse after seamount subduction (Dominguez *et al.* 2000; Wang & Bilek 2011), the Iquique Ridge subduction can explain the widening of the frontal unit north of ∼20°30′S by the fracturing and collapse of the frontal portion of the wedge. This mechanism likely contributes to the general decrease in density below the middle slope. On the other hand, the tectonic effect of ridge subduction beneath the shelf area is probably higher in the northern portion of the studied zone.

The width and obliquity of the Iquique Ridge indicate that its subduction trace is currently below the Arica Basin, and thus not affecting the continental shelf south of ∼19°30′S. In other words, the area of the Iquique basin is probably not tectonically affected by the subduction of this ridge (Fig. 9b). However, we cannot rule out the possibility of the subduction of an ancient oceanic relief, such as an isolated seamount not directly associated with the Iquique Ridge, as posited by Geersen *et al.* (2015), who interpreted the subduction of a seamount below the MLS limit in three seismic lines, north of 21°S. However, the apparent north–south continuity of those features suggests a probable relation between them and the large north–south horst-graben structures associated with the outer rise flexure of the slab (Figs 1 and 2). In this sense, León-Ríos *et al.* (2016) show a possible relationship between the subducted horst-graben structures and the high-dip focal mechanism of the Iquique earthquake aftershocks, which highlights the importance of these structures in the deformation process.

5.3 Implications for the Iquique earthquake and northern Chile seismic gaps

The relocated seismicity and coseismic slip models indicate that the coseismic rupture stopped at the frontal low-density unit and that this unit is characterized by the absence of foreshock and aftershock seismicity (Figs 2, 5, 9a). This suggests that the base of the frontal portion of the continental wedge can act as an aseismic contact, i.e. it can dissipate coseismic deformation in a way similar to that observed in the accretionary prism along accretionary margins (Contreras-Reyes *et al.* 2010, 2017). Landward, the SB corresponds to an important morphotectonic limit of the marine forearc (e.g. Contreras-Reyes *et al.* 2015, 2016, 2017; Becerra *et al.* 2017), and therefore, density variations can be explained by changes in rheology between two different structural domains (middle slope and continental shelf). Coincidentally, the location of the largest interplate foreshock of the Iquique earthquake sequence (M_w 6.7, see Figs 1, 2 and 9a) is aligned with the density change of the SB, and also with the presence of a first-order tectonic limit (F2) interpreted

in the seismic reflection lines around the area (Figs 4 and 5). Furthermore, one of the nodal planes of the largest interplate foreshock has a dip near 70 deg with an east vergency, which suggests that F2 was activated before the main shock.

Numerous swarms and repeater events generated before the main event were located below the middle slope (Ruiz *et al.* 2014; Meng *et al.* 2015; Kato *et al.* 2016), in the transition zone defined here; this could be related to an increase in fracturing and/or fluid content in the upper zone of the seismogenic contact. According to this, the coseismic rupture should be stopped upwards in the less-coupled transition zone and/or below the aseismic frontal unit (Figs 2 and 9a).

The observation of a structural and seismotectonic segmentation of the wedge in the direction perpendicular to the margin gives new perspectives to analyse the seismic cycle. If we note that the focal mechanism of the M_w 6.7 foreshock describes a high-angle reverse fault, and that the faults associated with F2 have a clear extensional character at long temporal scales (Fig. 4), then it is possible to interpret the mechanics of this tectonic limit during the seismic cycle as a response to continental wedge segmentation. In fact, following the works of Hyndman & Wang (1993), Farías *et al.* (2011), Contreras-Reyes *et al.* (2015), among others, the polarity of faults inside the continental wedge can be inverted during the interseismic and coseismic periods, according to the differential activation of coupled zones within the contact. The pre-seismic slow-slip event activated the zone where the coseimic slip was located about 20 d later (Ruiz *et al.* 2014; Socquet *et al.* 2017). Therefore, if the frontal aseismic unit, and probably part of the transition zone, remains coupled, the F2 limit could be activated by a high-angle reverse fault (M_w 6.7 foreshock event) in response to the resistance of the frontal portion of the continental wedge (see grey arrows in the interpretation schema, Fig. 9a). On the other hand, during the interseismic period, the frontal unit is probably deformed aseismically, and the transition zone remains under a relatively low-coupling zone, which favours the collapse of the frontal portion of the wedge. This stress change, in addition to the tectonic erosion process, can explain the normal long-term polarity of F2 and other structural limits of the upper plate.

The downward projection of the SB, F2 and the high-dip plane of the M_w 6.7 foreshock seems to correlate with a change in the foreshock and aftershock seismicity patterns, where the amount of seismicity decreases from the SB downwards. Also, it can be seen that the updip limit of the coseismic rupture area was located between the frontal unit and the SB-F2 limit. These observations define a 'transition zone' in the interplate boundary below the middle slope, characterized by the location of the Iquique earthquake updip limit, high seismicity and a smooth landward increase in continental density in comparison to the frontal unit, but more pronounced than that observed below the shelf (Figs 6a and 9a).

A parameter directly associated with friction is the normal stress on the megathrust. The horizontal stress field, related to the convergence process, and the vertical stress generated mainly by gravity, are components of this normal stress. However, in zones with a small subduction angle (<∼10 deg, as below the marine forearc, see Fig. 5), the main component is approximately vertical. Then, the observed values for vertical load over the seismogenic contact are reasonable estimates of normal stress and its variations in the upper portion of the subduction zone (depth <∼20 km).

Figs 6(b) and 7(b) show that the vertical load varies up to 150 MPa along the margin, which represents between 10 and 30 per cent of the average values observed in the study zone. While the vertical load below the frontal unit is highly variable (Fig. 6b), it presents

high values south of ∼20°30′S, below the shelf, and in particular two local highs below the middle slope [around 20°30′S, and in the zone of the Mejillones peninsula (Fig. 9b)].

Considering the previous analysis, the Iquique earthquake sequence (including coseismic rupture and foreshocks) was limited to the south by an increase in vertical load, which acted as a strong barrier. Therefore, we propose that the northern and southern regions have different seismic histories. The large southern seismic gap (unruptured since the 1877 earthquake), is limited to the south by a strong frictional barrier at the latitude of the Mejillones Peninsula. According to seismological records, this southern barrier also corresponded to the northern limit of the 1995 M_w 8.1 Antofagasta earthquake, and the southern limit of the down-dip 2007 M_w 7.7 Tocopilla earthquake (Bilek, 2010; Contreras-Reyes *et al.* 2012; Béjar-Pizarro *et al.* 2013), which could evidence the importance of this strong frictional barrier for large earthquake sequences.

Following models of interseismic coupling (Ruiz *et al.* 2014; Metois *et al.* 2016, among others), the southern segment (from ∼20°30′S to the Mejillones Peninsula) is currently coupled, and then a possible future scenario is the generation of a large earthquake rupturing the entire segment. However, a more complex seismic sequence can be suggested, where the observed strong barriers (at ∼20°30′S and 23°S) and the relative low vertical load between them could define a second-order segmentation where medium-sized earthquakes can rupture independently in the north, centre and south of the current large southern seismic gap.

The northern seismic gap comprises the zone from the Iquique earthquake to the southern limit of the 2001 M_w 8.4 southern Peru earthquake (∼18°S). As discussed before, there is a match between this gap and the alignment of the Iquique Ridge subducted track, the large Arica forearc basin and the Arica Bend, suggesting a different mechanical behaviour in comparison to the Iquique earthquake segment and the southern gap. According to Montessus de Ballore (1911–1916) and Comte & Pardo (1991), the area north of ∼23°30′S was affected by several moderate and giant earthquakes, which indicates a complex megathrust activation sequence. Considering the uncertainties in the ruptures of historical earthquakes, the limit between the current northern gap and the Iquique earthquake could have an important significance for the seismic sequence. In particular, if we propose that the fracturing associated with the Arica Bend, jointly with the Iquique ridge subduction, worked as a barrier for coseismic slip in 1877, then the current northern seismic gap could be a persistent feature of the margin.

Ruptures of giant earthquakes can propagate across barriers, and considering that some historical earthquakes might have been located in the deeper portion of the plate interface, the proposed scenarios are highly speculative. However, they are useful as case studies to evaluate the seismic hazard of the studied zone. Furthermore, regardless of the temporal sequence and size of large earthquakes in the area, the relatively small frontal sedimentary/fractured rock unit observed along the southern segment favours the upward propagation of coseismic ruptures, and the generation of large tsunamis in comparison to similar ruptures located north of ∼23°30′S. This aspect should be considered in future estimations of tsunami hazard for the region.

in upper plate density to the north, which suggests a northward increase in fracturing within and below the continental wedge. The observed rheological change can be explained as a response to the complex stress–strain fields around the Arica Bend, and also by the subduction of the Iquique ridge, which should intensify upper plate fracturing.

South of the Iquique earthquake rupture, the current southern seismic gap is extended between two local barriers of high normal stress (vertical load over the seismogenic contact), located at 20°30′S-21°S and at the latitude of the Mejillones Peninsula (∼23°S). Inside this segment, the calculated vertical load is high, at least below the shelf. In contrast, north of 20°30′S, normal stress is low and any increase in this parameter is correlated with the northern limit of the rupture. However, the alignment of the subducted Iquique Ridge hotspot track, the decrease in seismicity, and the development of the large Arica forearc basin, suggest differences in the crustal mechanical behaviour of the current northern seismic gaps (north of ∼19°30S). In this case, the northern limit of the Iquique earthquake could correspond to a weak barrier.

This study shows that the continental wedge is characterized by a landward decrease in porosity and fracturing. Lateral density gradients inside the continental wedge allow defining three main units: (1) a frontal unit made of debris and highly fractured rock, characterized by a rapid landward decrease in fracturing, (2) a transition zone, roughly correlated with the middle continental slope, where the fracturing degree decreases slowly landwards, and (3) a dense basement below the continental shelf. The frontal aseismic unit is narrower in the southern portion of the margin (20°30′S–23°S), which favours the generation of large tsunamis.

Seismicity associated with the 2014 Iquique earthquake shows that the frontal unit worked as an aseismic barrier, while during the updip of the main event numerous aftershocks and foreshocks were observed in the transition segment. According to the seismic reflection profiles, the limit between the transition segment and the shelf corresponds to an important landward-verging normal structure, which seems to have been activated during the largest M_w 6.7 intraplate foreshock. According to this, detailed studies of microseismicity should be done in the future in order to confirm the current seismic activity of these (and other) large continental structures within the continental wedge.

Assuming that the slow slip process was coincident with the coseismic rupture area, the mechanical resistance of the aseismic frontal unit and part of the transition zone could explain the activation of the landward limit of the transition zone as a high-angle reverse fault before the main event.

Our results show that variations in fracturing and tectonic style within the continental wedge have a large impact on the normal stress on the seismogenic contact, generating variations of up to 150 MPa in some places. These changes, together with the variable rheological conditions at the contact (friction coefficient, fluid pressure) result in a seismic segmentation of the Northern Chile subduction margin, where mechanically differentiated segments can be activated in a complex sequence of large events ($M_w \sim 8$), and jointly during giant earthquakes ($M_w > 8.5$).

6 SUMMARY AND CONCLUSIONS

The southern limit of the Iquique 2014 earthquake sequence correlates with an abrupt southward increase in offshore free-air gravity at ∼20°30′S. This strong change is explained by a general increase

REFERENCES

Angermann, D., Klotz, J. & Reigber, C., 1999. Space-geodetic estimation of the Nazca–South America Euler vector, *Earth planet. Sci. Lett.,* **171**(3), 329–334.

Armijo, R., Lacassin, R., Coudurier-Curveur, A. & Carrizo, D., 2015. Coupled tectonic evolution of Andean orogeny and global climate, *Earth Sci. Rev.,* **143**, 1–35.

Arriagada, C., Roperch, P., Mpodozis, C. & Cobbold, P.R., 2008. Paleogene building of the Bolivian Orocline: tectonic restoration of the Central Andes in 2-D map view, *Tectonics,* **27**(6).

Bassett, D., Sandwell, D.T., Fialko, Y. & Watts, A.B., 2016. Upper–plate controls on co-seismic slip in the 2011 magnitude 9.0 Tohoku-oki earthquake, *Nature,* **531**, 92–96.

Becerra, J., Arriagada, C., Contreras-Reyes, E., Bascuñan, S., De Pascale, G., Reichert, C., Diaz-Naveas, J. & Cornejo, N., 2017. Gravitational deformation and inherited structural control on slope morphology in the subduction zone of north-central Chile (∼29–33° S), *Basin Res.,* **29**(6), 798–815.

Bilek, S.L., 2010. Seismicity along the South American subduction zone: review of large earthquakes, tsunamis, and subduction zone complexity, *Tectonophysics,* **495**(1-2), 2–14.

Birch, F., 1961a. The velocity of compressional waves in rocks to 10 kilobars (Part I), *J. geophys. Res.,* **65**, 1083–1102.

Birch, F., 1961b. The velocity compressional waves in rocks to 10 kilobars (Part2), *J. geophys. Res.,* **66**, 2199–2224.

Blakely, R.J., 1995. *Potential Theory in Gravity and Magnetic Applications,* Cambridge Univ. Press.

Bonnardot, M.-A., Hassani, R., Tric, E., Ruellan, E. & Régnier, M., 2008. Effect of margin curvature on plate deformation in a 3-D numerical model of subduction zones, *Geophys. J. Int.,* **173**(3), 1084–1094.

Béjar-Pizarro, M., Socquet, A., Armijo, R., Carrizo, D., Genrich, J. & Simons, M., 2013. Andean structural control on interseismic coupling in the North Chile subduction zone, *Nat. Geosci.,* **6**(6), 462–467.

Casquet, C., Hervé, F., Pankhurst, R.J., Baldo, E., Calderón, M., Fanning, C.M., Rapela, C.W. & Dahlquist, J. 2014. The Mejillonia suspect terrane (Northern Chile): late Triassic fast burial and metamorphism of sediments in a magmatic arc environment extending into the Early Jurassic, *Gondwana Res.,* **25**, 1272–1286.

Cesca, S., Grigoli, F., Heimann, S., Dahm, T., Kriegerowski, M., Sobiesiak, M., Tassara, C. & Olcay, M., 2016. The M_w 8.1 2014 Iquique, Chile, seismic sequence: a tale of foreshocks and aftershocks, *Geophys J. Int.,* **204**(3), 1766–1780.

Charrier, R., Pinto, L. & Rodriguez, M.P., 2007. Tectonostratigraphic evolution of the Andean Orogen in Chile, in *Geology of Chile,* pp. 21–114, Geological Society Special Publication.

Clift, P. & Vannucchi, P., 2004. Controls on tectonic accretion versus erosion in sub-duction zones: implications for the origin and recycling of the continental crust, *Rev. Geophys.,* **42**, RG2001.

Comte, D. & Pardo, M., 1991. Reappraisal of great historical earthquakes in the northern Chile and southern Peru seismic gaps, *Nat. Hazards,* **4**, 23–44.

Contreras-Reyes, E. & Carrizo, D., 2011. Control of high oceanic features and sub-duction channel on earthquake ruptures along the Chile–Peru subduction zone, *Phys. Earth planet. Inter.,* **186**, 49–58.

Contreras-Reyes, E., Flueh, E.R. & Grevemeyer, I., 2010. Tectonic control on sediment accretion and subduction off south central Chile: implications for coseismic rupture processes of the 1960 and 2010 megathrust earthquakes, *Tectonics,* **29**.

Contreras-Reyes, E. & Garay, J., 2018. Flexural modeling of the elastic lithosphere at an ocean trench: a parameter sensitivity analysis using analytical solutions, *J. Geodynamics.,* **113**, 1–12.

Contreras-Reyes, E., Grevemeyer, I.,Watts A.B., Flueh, E.R., Peirce, C., Moeller, S. & Papenberg, C., 2011. Deep seismic structure of the Tonga subduction zone: Implications for mantle hydration, tectonic erosion, and arc magmatism, *J. geophys. Res.,* **116**(B10103), doi:10.1029/2011JB008434.

Contreras-Reyes, E., Jara, J., Grevemeyer, I., Ruiz, S. & Carrizo, D., 2012. Abrupt change in the dip of the subducting plate beneath north Chile, *Nat. Geosci.,* **5**, 342–345.

Contreras-Reyes, E., Maksymowicz, A., Lange, D., Grevemeyer, I., Muñoz-Linford, P. & Moscoso, E., 2017. On the relationship between structure, morphology and large coseismic slip: a case study of the M_w 8.8 Maule, Chile 2010 earthquake, *Earth planet. Sci. Lett.,* **478**, 27–39.

Contreras-Reyes, E., Voelker, D., Bialas, J., Moscoso, E. & Grevemeyer, I., 2016. Reloca Slide: an ∼24 km³ submarine mass wasting event in response to over-steepening and failure of the central Chilean continental slope, *Terra Nova,* **28**, 257–264.

Contreras-Reyes, E., Ruiz, J., Becerra, J., Kopp, H., Reichert, C., Makysymowicz, A. & Arriagada, C., 2015. Structure and tectonics of the central Chilean margin (31°–33° S): Implications for subduction erosion and shallow crustal seismicity, *Geophys. J. Int.,* **203**, 776–791.

Dominguez, S., Malavieille, J. & Lallemand, S.E., 2000. Deformation of accretionary wedges in response to seamount subduction: insights from sand-box experiments, *Tectonics,* **19**(1), 182–196.

Duputel, Z. *et al.*, 2015. The Iquique earthquake sequence of April 2014: Bayesian modeling accounting for prediction uncertainty, *Geophys. Res. Lett.,* **42**(19), 7949–7957.

Farias, M., Comte, D., Roecker, S., Carrizo, D. & Pardo, M., 2011. Crustal extensional faulting triggered by the 2010 Chilean earthquake: the pichilemu seismic sequence, *Tectonics,* **30**(6),

Geersen, J., Ranero, C.R., Barckhausen, U. & Reichert, C., 2015. Subducting seamounts control interplate coupling and seismic rupture in the 2014 Iquique earthquake area, *Nat. Commun.,* **6**, 8267.

González, G., Salazar, P., Loveless, J.P., Allmendinger, R.W., Aron, F. & Shrivastava, M., 2015. Upper plate reverse fault reactivation and the unclamping of the megathrust during the 2014 northern Chile earthquake sequence, *Geology,* **43**, 671–674.

Hamilton, E.L., 1978. Sound velocity–density relations in sea floor sediments, *J. acoust. Soc. Am.,* **63**, 366–377.

Hayes, G.P., Wald, D.J. & Johnson, R.L., 2012. Slab1.0: a three-dimensional model of global subduction zone geometries, *J. geophys. Res.,* **117**.

Hayes, G. P. *et al.*, 2014. Continuing megathrust earthquake potential in Chile after the 2014 Iquique earthquake, *Nature,* **512**(7514), 295–298.

Hunter, J. & Watts, A.B., 2016. Gravity anomalies, flexure and mantle rheology seaward of circum-Pacific trenches, *Geophys. J. Int.,* **207**, 288–316 .

Hyndman, R.D. & Wang, K., 1993. Thermal constraints on the zone of major thrust earthquake failure: the Cascadia subduction zone, *J. geophys. Res.,* **98**(B2), 2039–2060.

Isacks, B. L., 1988. Uplift of the Central Andean Plateau and bending of the Bolivian oroncline, *J. geophys. Res.,* **93**, 3211–3231.

Jarvis, A., Reuter, H.I., Nelson, A. & Guevara, E., 2008. Hole-filled SRTM for the globe Version 4, available from the CGIAR-CSI SRTM 90 m Database. http://srtm.csi.cgiar.org.

Kato, A., Fukuda, J., Kumazawa, T. & Nakagawa, S., 2016. Accelerated nucleation of the 2014 Iquique, Chile M_w 8.2 earthquake, *Sci. Rep.,* **6**, 24792.

Lallemand, S.E., Schnurle, P. & Malavieille, J., 1994. Coulomb theory applied to accretionary and nonaccretionary wedges—possible causes for tectonic erosion and/or frontal accretion, *J. geophys. Res.,* **99**, 12 033–12 055.

Lengliné, O., Lamourette, L., Vivin, L., Cuenot, N. & Schmittbuhl, J., 2014. Fluid-induced earthquakes with variable stress drop, *J. Geophys. Res.,* **119,** 8900–8913.

León-Ríos, S., Ruiz, S., Maksymowicz, A., Leyton, F., Fuenzalizada, A. & Madariaga, R., 2016. Diversity of the Iquique's foreshocks and aftershocks: a clue about complex rupture process of a M_w 8.1 earthquake, *J. Seismol.,* **20,** 1059–1073.

Loveless, J.P., Pritchard, M.E. & Kukowski, N., 2010. Testing mechanisms of subduction zone segmentation and seismogenesis with slip distributions from recent Andean earthquakes, *Tectonophysics,* **495,** 15–33.

Lüke, O.H. & Arroyo, I.G., 2015. Density structure and geometry of the Costa Rican subduction zone from 3-D gravity modeling and local earthquake data, *Solid Earth,* **6,** 1169–1183, doi:10.5194/se-6-1169-2015.

Madella, A., Delunel, R., Audin, L. & Schlunegger, F., 2016. Why is there no Coastal Cordillera at the Arica Bend (Western Central Andes)? *Basin Res.,* **30,** 248–268.

Maksymowicz, A., Trehu, A., Contreras-Reyes, E. & Ruiz, S., 2015. Density-depth model of the continental wedge at the maximum slip segment of the Maule Mw8.8 megathrust earthquake, *Earth planet. Sci. Lett.,* **409,** 265e277.

Melnick, D., 2016. Rise of the central Andean coast by earthquakes straddling the Moho, *Nat. Geosci.,* **9,** 401–407.

Meng, L., Huang, H., Bürgmann, R., Ampuero, J.P. & Strader, A., 2015. Dual megathrust slip behaviors of the 2014 Iquique earthquake sequence, *Earth planet Sci. Lett.,* **411,** 177–187.

Mochizuki, K., Yamada, T., Shinohara, M., Yamanaka, Y. & Kanazawa, T., 2008. Weak interplate coupling by seamounts and repeating M 7 earthquakes, *Science,* **321,** 1194–1197.

Montessus de Ballore, F., 1911–1916. *Historia Sísmica de los Andes Meridionales, al sur del Paralelo XVI,* Cervantes.

Métois, M., Vigny, C. & Socquet, A., 2016. Interseismic coupling, megathrust earthquakes and seismic swarms along the Chilean Subduction Zone (38°–18°S), *Pure appl. Geophys.,* **173,** 1431–1449.

Métois, M. *et al.*, 2013. Revisiting the North Chile seismic gap segmentation using GPS derived interseismic coupling, *Geophys. J. Int.,* **194,** 1283–1294.

Oliveros, V., Féraud, G., Aguirre, L., Fornari, M. & Morata, D. 2006. The Early Andean Magmatic Province (EAMP): $^{40}Ar/^{39}Ar$ dating on Mesozoic volcanic and plutonic rocks from the Coastal Cordillera, northern Chile, *J. Volc. Geotherm. Res.,* **157,** 311–330

Oliveros, V., Morata, D., Aguirre, L., Féraud, G. & Fornari, M., 2007. Jurassic to Early Cretaceous subduction-related magmatism in the Coastal Cordillera of northern Chile (18°30′–24° S): Geochemistry and petrogenesis, *Revista Geológica de Chile,* **34,** 209–232.

Oncken, O. *et al.*, 2003. Seismic imaging of a convergent continental margin and plateau in the central Andes (Andean Continental Research Project 1996 (ANCORP' 96)), *J. geophys. Res.,* **108,** 2328.

Poli, P., Maksymowicz, A. & Ruiz, S., 2017. The M_w 8.3 Illapel earthquake (Chile): Preseismic and postseismic activity associated with hydrated slab structures, *Geology,* **45,** 247–250.

Reichert, C., 1997. Chr. Reporter Results of the marine geo-scientific survey so-104/CINCA, in *Congreso Geológico Chileno,* **8,** pp. 1818–1822, Antofagasta, Chile, 13–17 Octubre.

Reutter, K.-J. & Munier, K., 2006. Digital geological map of the Central Andes between 20° S and 26° S, in *The Andes - Active Subduction Orogeny. Frontiers in Earth Sciences 1,* eds Oncken, O., Chong, G., Franz, G., Giese, P., Götze, H.-J., Ramos, V., Strecker, M. & Wigger, P., Springer.

Robinson, D.P., Das, S. & Watts, A.B., 2006. Earthquake rupture stalled by a subducting fracture zone, *Science,* **312,** 1203–1205.

Ruiz, S. *et al.*, 2014. Intense foreshocks and a slow slip event preceded the 2014 Iquique M_w 8.1 earthquake, *Science,* **345**(6201), 1165–1169.

Sallares, V. & Ranero, C.R., 2005. Structure and tectonics of the erosional convergentmargin off Antofagasta, north Chile (23°30′S), *J. geophys. Res.,* **110,** B06101.

Sandwell, D.T. & Smith, W.H.F., 2009. Global marine gravity from retracked Geosat and ERS-1 altimetry: Ridge Segmentation versus spreading rate, *J. geophys. Res.,* **114,** B01411.

Schurr, B. *et al.*, 2014. Gradual unlocking of plate boundary controlled initiation of the 2014 Iquique earthquake, *Nature,* **512,** 299–302.

Smith, W.H.F. & Sandwell, D.T., 1997. Global seafloor topography from satellite altimetry and ship depth soundings, *Science,* **277,** 1957–1962.

Socquet, A. *et al.*, 2017. An 8 month slow slip event triggers progressive nucleation of the 2014 Chile megathrust, *Geophys. Res. Lett.,* **44**(9), 4046–4053.

Song, T.A. & Simons, M., 2003. Large trench-parallel gravity variations predict seismo-genic behavior in subduction zones, *Science,* **301,** 630–633.

Sparkes, R., Tilmann, F., Hovius, N. & Hillier, J., 2010. Subducted seafloor relief stops rupture in South American great earthquakes: implications for rupture behaviour in the 2010 Maule, Chile earthquake, *Earth planet. Sci. Lett.,* **298**(1–2), 89–94.

Tréhu, A.M., Blakely, R.J. & Williams, M.C., 2012. Subducted seamounts and recent earthquakes beneath the central Cascadia forearc, *Geology,* **40,** 103–106, doi: 10.1130/G32460.1.

Vannucchi, P., Sage, F., Morgan, J.P., Remitti, F. & Collot, J.Y., 2012. Toward a dynamic concept of the subduction channel at erosive convergent margins with implications for interplate material transfer, *Geochem. Geophys. Geosyst.,* **13,** Q02003.

von Huene, R. & Scholl, D.W., 1991. Observations at convergent margins concerning sediment subduction, subduction erosion, and the growth of continental crust, *Rev. Geophys.,* **29**(3), 279–316.

Wang, K. & Bilek, S.L., 2011. Do subducting seamounts generate or stop earthquakes? *Geology,* **39,** 819–822.

Wells, R.E., Blakely, R.J., Sugiyama, Y., Scholl, D.W. & Dinterman, P.A., 2003. Basin-centered asperities in great subduction zone earthquakes: a link between slip, subsidence, and subduction erosion? *J. geophys. Res.,* **108**(B10), 2507.

Yagi, Y., Okuwaki, R., Enescu, B., Hirano, S., Yamagami, Y., Endo, S & Komoro, T., 2014. Rupture process of the 2014 Iquique Chile earthquake in relation with the foreshock activity, *Geophys. Res. Lett.,* **41**(12), 4201–4206.

Yuan, X., et. al., 2000. Subduction and collision processes in the Central Andes constrained by converted seismic phases, *Nature,* **408,** 958–961.

Álvarez, O., Nacif, S., Spagnotto, S., Folguera, A., Giménez, M., Chlieh, M. & Raitenberg, C., 2015. Gradients from GOCE reveal gravity changes before Pisagua M_w = 8.2 and Iquique M_w = 7.7 large megathrust earthquakes, *J. South Am. Earth Sci.,* **64**(2), 273–287.

SUPPORTING INFORMATION

Supplementary data are available at *GJI* online.

Figure S1. Interpretation of the ENAP seismic lines. The sedimentary fill is highlighted in orange and the fault zones are indicated in black. F1, F2 and F3 are the main tectonic limits identified, which show apparent continuity between adjacent lines.

Figure S2. Empirical conversion from TWT to depth. (a) Available interval velocity data as a function of the depth at the middle of each layer. (b) Empirical law (blue line) for the depth (below the bathymetry) as a function of TWT calculated from the data (red dots).

Figure S3. 3-D representation of the sedimentary fill. Red dots are the seafloor and basement elevation observed in the ENAP seismic reflection profiles. Green dots are the seafloor and basement elevation observed in the SO104 seismic reflection profiles. Black lines correspond to the bathymetry along the modelled gravimetric profiles P1–P7. Dotted blue lines indicate the main crustal tectonic limits interpreted in seismic profiles and bathymetry, and dotted black line is the limit between lower and middle slope. Black vertical arrows indicate the epicentre of the main shock (M_w 8.2) and the large foreshock and aftershock (M_w 6.7 and M_w 7.7, respectively).

Figure S4. Density-depth models along gravity model profiles. For each profile (P1–P11), the upper panel presents the observed gravity

from the gravimetric stations (black dots), and the cyan line shows the complementary Sandwell and Smith satellite data. The red line corresponds to the modelled free-air gravity anomaly. The lower panels present the corresponding 2-D density model.

Figure S5. Gravity response in line P4 due to slab geometry changes. (a) Black dots are the observed Free-air gravity data, red line is the gravity response of the preferred density model and blue lines are the gravity response considering upward and downward modifications of the slab geometry. (b) Modified density model considering an upward variation of the slab geometry. (c) Preferred density model. Blue lines are the modified models of slab presented in (b) and (d). (d) Modified density model considering a downward variation of the slab geometry.

Figure S6. Gravity response in line P4 due to changes in the upper continental density. (a) Black dots are the observed Free-air gravity data, red line is the gravity response of the preferred density model and blue lines are the gravity response considering an increase and a decrease of the upper continental density. (b) Modified density model considering an increase of the upper continental density. (c) Preferred density model. (d) Modified density model considering a decrease of the upper continental density.

Figure S7. Gravity response in line P4 due to changes in the lower continental density. (a) Black dots are the observed Free-air gravity data, red line is the gravity response of the preferred density model and blue lines are the gravity response consid-

ering an increase and a decrease of the lower continental density. (b) Modified density model considering an increase of the lower continental density. (c) Preferred density model. (d) Modified density model considering a decrease of the lower continental density.

Figure S8. Average density and vertical load over the interplate boundary of the perturbed density models of the line P4. (a) Vertical average density of the continental wedge as a function of distance from the trench. (b) Vertical load over the interplate boundary as a function of distance from trench.

Figure S9. Seismicity along the northern-Chile margin. The figure presents the catalogue of the Chilean Seismological Center (Servicio Simológico Nacional, CSN). Circles in the left-hand panel show the latitude and time of the events and black arrows highlight some specific latitudes where seismicity is persistent in time. The right-hand panel presents the Free-air anomaly and some important features of the margin (see main text for details). Horizontal light-red band corresponds to a segment of the margin with relatively low seismicity, which correlates with the position of the Arica-basin in the marine forearc.

Please note: Oxford University Press is not responsible for the content or functionality of any supporting materials supplied by the authors. Any queries (other than missing material) should be directed to the corresponding author for the paper.